Chinese Chemical Letters 37 (2026) 112442

Contents lists available at ScienceDirect

Chinese Chemical Letters

journal homepage: www.elsevier.com/locate/cclet

Engineering amorphous MOF with P–Fe–O sites for robust electro-Fenton degradation of micropollutants

Pan Xia[a,1], Chuanzhu Tang[a,1], Tong Xu[a], Pinyuan Sheng[a], Liyuan Liu[b], Chao Wang[a], Yin Xu[b], Qiang He[a], Ömür Gökkuş[c], Zhihong Ye[a,*]

[a] College of Environment and Ecology, Key Laboratory of Eco-environments in Three Gorges Reservoir Region, Ministry of Education, Chongqing University, Chongqing 400045, China
[b] Hubei Key Laboratory of Regional Development and Environmental Response, Faculty of Resources and Environmental Science, Hubei University, Wuhan 430062, China
[c] Department of Environmental Engineering, Sivas Cumhurivet University, 58140 Sivas, Turkey

ARTICLE INFO

Article history:
Received 18 September 2025
Revised 25 November 2025
Accepted 21 January 2026
Available online 22 January 2026

Keywords:
Electro-Fenton
Amorphous MOF
MIL-88B(Fe)
P-coordination
Micropollutant degradation

ABSTRACT

Iron-based metal-organic frameworks (MOFs) stand out as promising catalysts for heterogeneous electro-Fenton (HEF) treatment of micropollutants, yet their performance is often constrained by the limited accessibility of active sites and sluggish electron transfer. Herein, a facile phosphine-assisted amorphization strategy was proposed to convert crystalline MIL-88B(Fe) into a P-coordinated amorphous counterpart (aMIL-88B(Fe)-P) featuring abundant asymmetric P–Fe–O moieties. The amorphous architecture ensures abundant exposure of active sites and enhanced mass transport, while the asymmetric coordination environment upshifts the Fe d-band center toward the Fermi level, thereby lowering the energy barrier for H_2O_2 activation. Notably, the aMIL-88B(Fe)-P-catalyzed EF system attained complete naproxen removal within 90 min, with a pseudo-first-order kinetic rate constant of 0.038 min^{-1}, outperforming all comparative trials and many reported HEF systems. Moreover, the system demonstrated broad-spectrum micropollutant removal, favorable catalyst reusability, and remarkable scalability in a flow-through electrochemical device, confirming strong practical applicability. This work highlights the potential of combining structural amorphization with precise coordination engineering to fully unlock the catalytic potential of MOFs for advanced EF applications.

© 2026 Published by Elsevier B.V. on behalf of Chinese Chemical Society and Institute of Materia Medica, Chinese Academy of Medical Sciences.

The electro-Fenton (EF) process, which involves *in-situ* H_2O_2 generation followed by hydroxyl radical ($^{\bullet}OH$, $E^0 = 2.8$ V *vs.* SHE) production *via* Fenton chemistry, has emerged as a promising technology for the degradation of recalcitrant organic pollutants owing to its high efficiency, environmental compatibility, and low operating cost [1,2]. In particular, heterogeneous EF (HEF) systems have gained increasing attention, as they circumvent several inherent limitations of homogeneous counterparts, including the need of acidic reaction pH (~3.0), generation of secondary iron sludge, and difficulty in catalyst reuse [3,4]. An ideal HEF catalyst should not only enable efficient and sustainable H_2O_2 activation but also maintain robust structural stability under long-term operation. Among various iron-based materials, metal–organic frameworks (MOFs), a class of porous crystalline materials composed of metal nodes and organic linkers, have recently emerged as promising candidates [5]. Their tunable architectures, high specific surface areas, and versatile coordination environments make them particularly attractive for enhancing mass transport and H_2O_2 activation in EF [6,7]. Specifically, iron-based metal-organic framework (Fe-MOFs), particularly MIL-88B(Fe), have demonstrated considerable potential in catalyzing heterogeneous Fenton and EF reactions due to the well-dispersed iron active sites and favorable water stability [8]. However, the catalytic performance of pristine MOFs remains unsatisfactory, largely owing to the intrinsic structural drawbacks such as close-ended polyhedron frameworks, pore blockage by guest molecules, overly rigid metal-ligand coordination, and poor electron transfer capacity [9]. These limitations underscore the urgent need for rational modification strategies to develop advanced Fe-MOF-based materials with enhanced catalytic activity and durability.

Benefiting from the high structural tunability of MOFs, two primary modification strategies have been extensively explored. The first is chemical functionalization, such as introducing electron-donating/withdrawing groups (*e.g.*, $-NH_2$, –COOH, $-SO_3H$), which

* Corresponding author.
E-mail address: yezhihong@cqu.edu.cn (Z. Ye).
[1] These authors contributed equally to this work.

https://doi.org/10.1016/j.cclet.2026.112442
1001-8417/© 2026 Published by Elsevier B.V. on behalf of Chinese Chemical Society and Institute of Materia Medica, Chinese Academy of Medical Sciences.

can alter the local electronic structure of Fe sites and potentially boost electron transfer during EF [10–12]. The second involves high-temperature pyrolysis, transforming MOFs into Fe-based carbonaceous materials with improved conductivity and greater availability of active modification often fails to overcome the inherently low catalytic activity of Fe centers constrained within the rigid crystalline active sites [13,14]. Although these approaches have achieved notable progress, they still present significant limitations. Chemical modification often fails to overcome the inherently low catalytic activity of Fe centers constrained within the rigid crystalline framework [15]. Pyrolysis is energy-intensive and typically results in metal site aggregation and the loss of intrinsic porosity and spatial architecture of MOFs [16]. Recently, amorphous MOFs have emerged as compelling alternatives to challenge the overwhelming dominance of crystalline counterparts [17,18]. These materials retain the basic building blocks and short-range connectivity of MOFs while eliminating the long-range periodicity, resulting in unique properties such as disordered atomic networks, absence of grain boundaries, high exposure of catalytic centers, and abundant structural defects [19]. Although still in an early stage of exploration, amorphous MOFs have shown considerable potential in electrocatalytic applications. For instance, Xu *et al.* [20] constructed an amorphous bimetallic MIL-88B with Zn–O–Fe linkages *via* a ligand-competition strategy. The resulting amorphous structure enhanced the accessibility of active sites, while the Zn–O–Fe secondary building units facilitated Fe^{3+}/Fe^{2+} redox cycling in EF process. Nevertheless, the transition to amorphous structures also introduces new challenges. The lack of crystallinity leads to structural heterogeneity, undefined active site configurations, and non-optimized charge transport pathways, which collectively hinder catalytic precision and long-term durability.

Recent advances have focused on the rational design of the coordination environment surrounding metal active centers through heteroatom doping and bimetallic node construction. The local electronic structure of metal sites can be finely tuned by engineering coordination asymmetry, thereby enhancing electron transfer efficiency and regulating the adsorption and transformation behavior of key reaction intermediates during the EF process [21–23]. For instance, Tan *et al.* [24] developed a hollow spherical carbon-supported asymmetric FeN_2O_2 single-atom catalyst, in which the substitution of nitrogen atoms with oxygen induced local charge redistribution and a downshift of the Fe d-band center compared to the FeN_4 moiety, thereby lowering the energy barrier for H_2O_2 activation. Qin *et al.* [25] proposed a Fe-Co dual-atomic-site catalyst to facilitate $^{\bullet}OH$ generation in EF, where the adjacent Co and Fe sites synergistically optimized the binding energies of key reaction intermediates. Notably, phosphorus (P) doping has been considered a particularly effective approach due to its larger atomic radius and lower electronegativity compared to N or O. The formation of unique metal–P coordination may break the symmetry of conventional Fe-O moieties in Fe-MOFs, potentially modulating the localized electronic states of Fe and thereby optimizing the adsorption behavior of the reactants and key intermediates during catalytic reactions [26,27].

Inspiringly, we have developed a novel P-coordinated amorphous MIL-88B(Fe) catalyst featuring abundant asymmetric P–Fe–O moieties (aMIL-88B(Fe)-P) *via* stepwise phosphine treatment and low-temperature heat treatment of the crystalline MIL-88B(Fe) precursor. The resulting aMIL-88B(Fe)-P was employed to construct a robust EF system for the degradation of naproxen (NPX) and other refractory micropollutants. The amorphization process enriched the density of accessible active sites and opened extensive mass transport channels. Meanwhile, the asymmetric P–Fe–O coordination modulated electron distribution and shifted the d-band center of Fe atoms, significantly enhancing electron transfer and lowering the energy barrier for H_2O_2 activation. As expected, these synergistic effects endowed the aMIL-88B(Fe)-P-catalyzed EF system with superior catalytic performance for micropollutant treatment. In addition, P incorporation contributed to stabilizing iron active sites, thereby compensating for the loss of crystallinity-induced structural robustness. The practical viability of the EF system was comprehensively demonstrated through pollutant degradation tests under varied water matrices and repeated operational cycles, together with scalable flow-through device integration and ecotoxicological evaluation of the treated effluent. Further electrochemical tests and theoretical calculations elucidated the underlying atomic-level mechanisms responsible for the enhanced H_2O_2 activation and pollutant degradation. Overall, this study highlights the promising strategy of integrating structural amorphization with precise coordination modulation to fully unlock the catalytic potential of MOFs for EF applications.

The synthetic process of aMIL-88B(Fe)-P is illustrated in Fig. 1a. Pristine MIL-88B(Fe) was fabricated *via* a hydrothermal method using a DMF solution containing ferric chloride ($FeCl_3{\cdot}6H_2O$) and terephthalic acid (H_2BDC). Phosphine-functionalized MIL-88B(Fe) (MIL-88B(Fe)-P) was subsequently obtained by treating MIL-88B(Fe) with an ethanol solution of triphenylphosphine (PPh_3). The coordination of PPh_3 to Fe nodes enabled heterogeneous grafting of organic ligands, thereby modifying the local microenvironment within the framework [28]. Upon heat treatment at 350 °C, solvent molecules were rapidly removed from the pores of MIL-88B(Fe)-P, generating internal capillary forces at the liquid–gas meniscus. These forces triggered structural collapse, inducing a crystalline-to-amorphous phase transition to form aMIL-88B(Fe)-P. The scanning electron microscopy (SEM) image of MIL-88B(Fe) reveals a uniform spindle-like morphology with an average particle length of approximately 1.0 μm and a diameter of 196 nm, indicative of its well-defined crystalline structure (Fig. 1b). Direct heat treatment of MIL-88B(Fe) disrupted its hexagonal morphology, yielding elongated spindle-shaped rods of similar size (Fig. 1c). Notably, numerous spherical particles are observed on the surface, likely due to the aggregation of Fe nodes in the absence of dispersion-stabilizing interactions during thermal treatment [29]. Nevertheless, high-resolution transmission electron microscopy (HRTEM) still reveals signatures of crystalline-to-amorphous transition. In contrast, aMIL-88B(Fe)-P exhibits pronounced structural disorder and a notable reduction in size (~703 nm in length and ~193 nm in width), without visible surface spherical particles (Fig. 1d). This significant size shrinkage is mainly attributed to the hydrophobic nature of PPh_3, which disrupts hydrogen bonding between solvent molecules and MOF framework, thereby weakening solvation forces and promoting structural contraction toward a more compact configuration [30]. Moreover, the strong coordinating ability of PPh_3 stabilizes the internal coordination environment, effectively suppressing the aggregation of surface-localized Fe species [31]. The corresponding HRTEM image and selected area electron diffraction (SAED) pattern show no distinct lattice fringes, confirming the successful formation of the amorphous phase. Elemental mapping in Fig. 1e further verifies the uniform distribution of Fe, P, O, and C, suggesting the absence of Fe aggregation during the heat treatment.

The thermal behavior of MIL-88B(Fe)-P was investigated by thermogravimetric analysis (TGA) over a temperature range of 50 to 800 °C. As illustrated in Fig. 1f, the TGA profile reveals four distinct weight-loss stages. The first stage, occurring between 50 and 338 °C, shows a weight loss of 19.2%, attributed to the gradual evaporation of physically adsorbed solvents and water molecules. The second stage, from 338 to 424 °C, accounts for a loss of 18.4 %, corresponding to the removal of chemisorbed solvent molecules and uncoordinated organic ligands, accompanied by the progressive transition from a crystalline to an amorphous structure. The third stage, between 424 and 566 °C, features a weight loss of

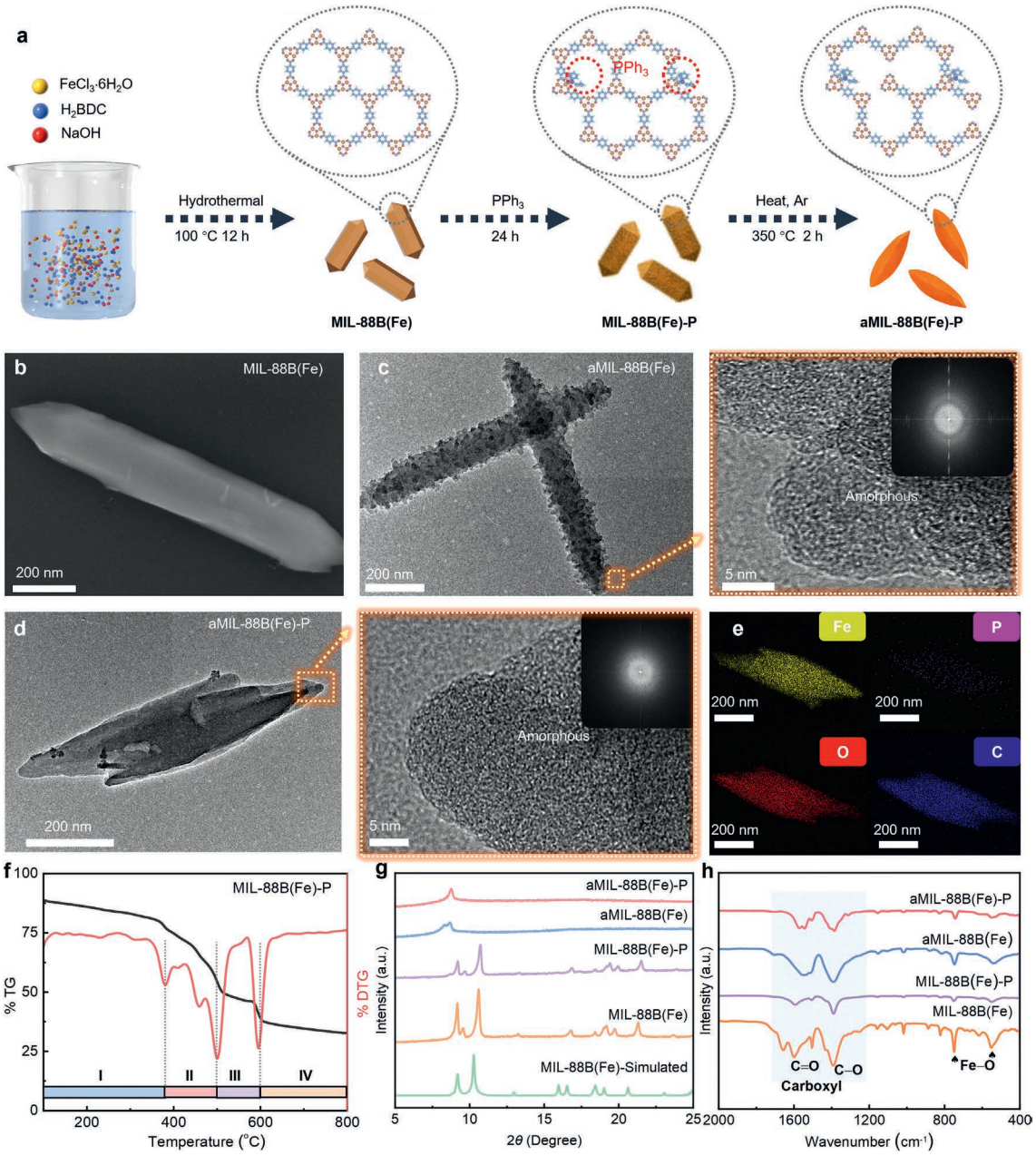


Fig. 1. (a) Schematic illustration of aMIL-88B(Fe)-P fabrication. (b) SEM image of MIL-88B(Fe). HRTEM images of (c) aMIL-88B(Fe) and (d) aMIL-88B(Fe)-P. (e) Elemental mapping of Fe, P, O and C in aMIL-88B(Fe)-P. (f) TG and DTG curves of MIL-88B(Fe)-P. (g) XRD patterns and (h) FTIR spectra of MIL-88B(Fe), MIL-88B(Fe)-P, aMIL-88(Fe), and aMIL-88B(Fe)-P.

16.1 %, associated with the significant collapse of the frameworks and the formation of iron oxides. Upon further heating to 800 °C, an additional weight loss of 13.7 % is observed, resulting from the extensive carbonization of organic components. Accordingly, 350 °C is validated as a viable temperature for the amorphization process.

The crystal structure and phase composition of the as-prepared materials were characterized by powder X-ray diffraction (XRD). As shown in Fig. 1g, the diffraction pattern of MIL-88B(Fe) closely matches the simulated spectrum (CCDC-285810), confirming its high crystallinity [32]. MIL-88B(Fe)-P exhibits an XRD pattern similar to that of the MIL-88B(Fe) precursor, indicating that PPh_3 functionalization does not induce lattice distortion. After heat treatment, the disappearance of the main Bragg peaks in both aMIL-88B(Fe) and aMIL-88B(Fe)-P suggests the loss of long-range order, evidencing successful amorphization [33]. The Fourier transform infrared (FTIR) spectra of the synthesized samples are shown in Fig. 1h. The sharp peaks at 1392 and 1600 cm^{-1} in MIL-88B(Fe) correspond to the stretching vibrations of carboxyl groups (–COO–) in the organic ligands, while the band at 545 and 750 cm^{-1} is attributed to the Fe–O vibrational mode arising from coordination between Fe nodes and H_2BDC [34,35]. These vibrational modes are retained in both MIL-88B(Fe)-P and the amorphous derivatives, indicating that neither phosphine functionalization nor amorphization disrupts the basic building blocks and connectivity. The nitrogen adsorption-desorption isotherms in Fig. S1a (Supporting information) illustrate a higher surface area of aMIL-88B(Fe)-P than that of the crystalline precursor (30.2 m^2/g *vs.* 25.4 m^2/g). Moreover, the amorphization treatment generated a higher amount of mesopores (10-40 nm), which can favor greater

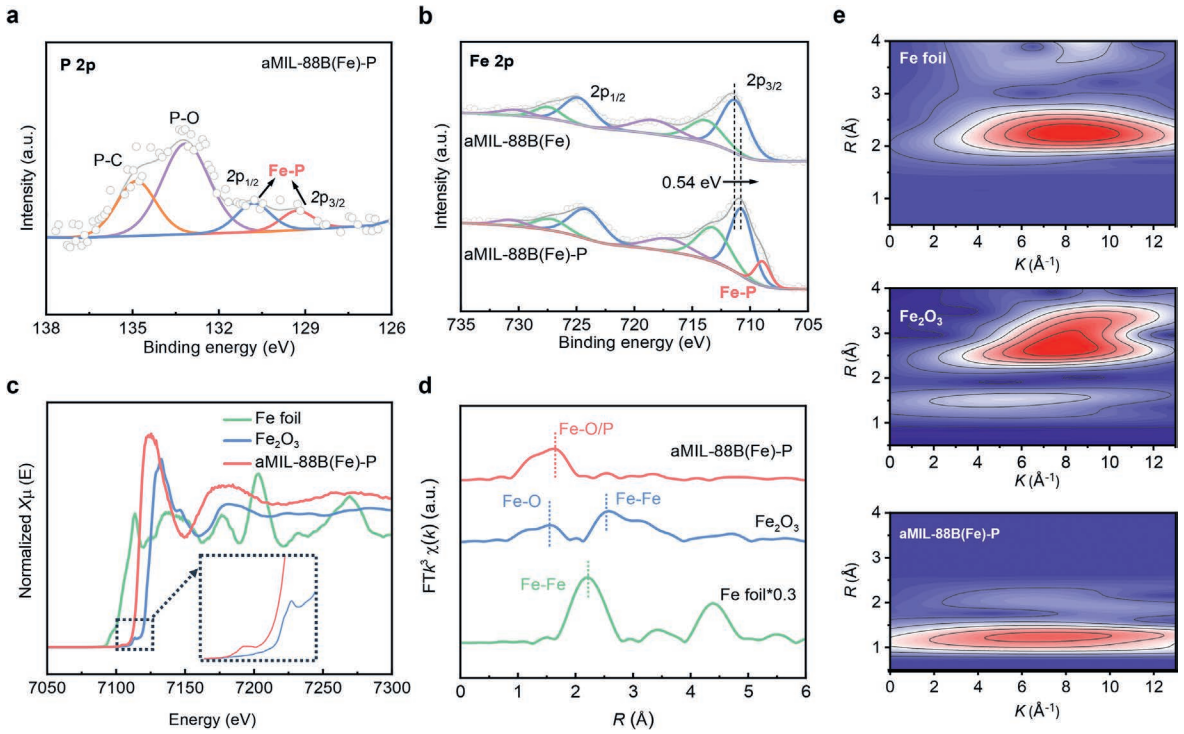


Fig. 2. (a) High-resolution XPS spectrum of P 2p for aMIL-88B(Fe)-P. (b) High-resolution XPS spectra of Fe 2p for aMIL-88B(Fe) and aMIL-88B(Fe)-P. (c) Fe K-edge XANES spectra and (d) Fourier-transformed (FT) k^3-weighted EXAFS spectra of aMIL-88B(Fe)-P and reference samples (Fe foil, Fe_2O_3). (e) Wavelet transform (WT) contour plots of Fe K-edge for Fe foil, Fe_2O_3 and aMIL-88B(Fe)-P.

exposure of active sites and enhanced molecular diffusion (Fig. S1b in Supporting information).

As a strong electron-donating organophosphate ligand, PPh_3 can undergo ligand exchange with coordinatively unsaturated sites in the MIL-88B(Fe) framework [36,37]. This coordination substitution disrupts the original Fe^{3+}–carboxylate bonds and alters the local coordination environment around the Fe centers in aMIL-88B(Fe)-P [38]. Thus, the chemical states and coordination nature of aMIL-88B(Fe)-P are further explored by X-ray photoelectron spectroscopy (XPS) and X-ray absorption spectroscopy (XAS). As illustrated in the P 2p XPS spectrum (Fig. 2a), two broad peaks at 131.1 and 134.9 eV are assigned to P–O and P–C bonds, respectively, while distinct peaks located at 129.1 and 130.8 eV correspond to the P component of Fe–P coordination [39]. Additionally, a peak centered at 709.0 eV in the high-resolution Fe 2p XPS spectrum of aMIL-88B(Fe)-P further confirms the presence of Fe–P bonding (Fig. 2b) [40]. Two other sets of fitting peaks corresponding to Fe $2p_{1/2}$ and Fe $2p_{3/2}$ bands are attributed to Fe(III) species. Specifically, the peaks at 724.9 and 711.4 eV are assigned to Fe(III) of Fe-O-C (BDC), while those at 727.6 and 714.0 eV are ascribed to Fe(III) of μ_3-OFe clusters [41]. Notably, all Fe(III)-related peaks exhibit slight positive shifts (~0.54 eV), indicating an increase in electron density around the Fe centers due to the electron-donating nature of the coordinated P atoms. The normalized Fe K-edge X-ray absorption near edge structure (XANES) spectra of aMIL-88B(Fe)-P and several standard references are shown in Fig. 2c. A distinct pre-edge peak at 7100.1 eV is observed for aMIL-88B(Fe)-P, corresponding to the dipole-forbidden Fe $1s \rightarrow 3d$ transition. This feature indicates that P doping induces local structural distortion and disrupts the original symmetric Fe–O coordination environment [42]. Moreover, the average oxidation state of Fe in aMIL-88B(Fe)-P is estimated to be approximately 3.0, consistent with the Fe 2p XPS results in Fig. 2b. The corresponding Fourier-transformed (FT) k^3-weighted extended X-ray absorption fine structure (EXAFS) spectra reveal a dominant peak at ~1.7 Å in aMIL-88B(Fe)-P, with no detectable Fe–Fe scattering (Fig. 2d). This peak lies between the typical backscattering distances for Fe–O and reported Fe–P bonds, suggesting the coexistence of both coordination paths [43–45]. Further wavelet transform (WT) EXAFS analysis reveals a contour maximum centered at 7.0 $Å^{-1}$ for aMIL-88B(Fe)-P, significantly different from that of the Fe_2O_3 reference (8.1 $Å^{-1}$). The broadened and shifted intensity relative to Fe_2O_3 suggests local geometric distortion, likely induced by P incorporation, which leads to the formation of asymmetric P–Fe–O configurations (Fig. 2e). These findings confirm that aMIL-88B(Fe)-P not only retains the basic metal–ligand blocks but also introduces P-based local coordination environments. The lower electronegativity of P facilitates electron donation to the Fe centers, thereby modulating the local electronic structure and potentially enhancing H_2O_2 activation performance.

To evaluate the catalytic performance of the synthesized catalysts in the EF system under near-neutral pH 5.0, NPX, a widely used non-steroidal anti-inflammatory drug, was selected as the model pollutant. As illustrated in Fig. S2 (Supporting information), the electro-oxidation process with *in-situ* H_2O_2 generation (denoted as EO-H_2O_2) using an IrO_2-based dimensionally stable anode (IrO_2-DSA) only achieved a modest NPX removal of 20.1 %, which can be attributed to the limited oxidative capacity of surface IrO_2(•OH) species [22]. Additionally, the physical adsorption of NPX by aMIL-88B(Fe)-P remained unsatisfactory (28.9 %). Although PPh_3 functionalization and heat treatment of MIL-88B(Fe) slightly improved NPX pre-adsorption, likely due to the partial replacement or removal of solvent and water molecules originally confined within the pristine pores (Fig. 3a). The MIL-88B(Fe)-catalyzed EF process showed enhanced NPX degradation (46.3 %), benefiting from •OH generation *via* the Fenton's reaction. Nevertheless, the limited availability of unsaturated Fe active sites in MIL-88B(Fe) hindered effective H_2O_2 activation for •OH production. Despite incorporating PPh_3 to tune Fe coordination, MIL-88B(Fe)-P exhibited even lower catalytic activity than its precursor, achieving only

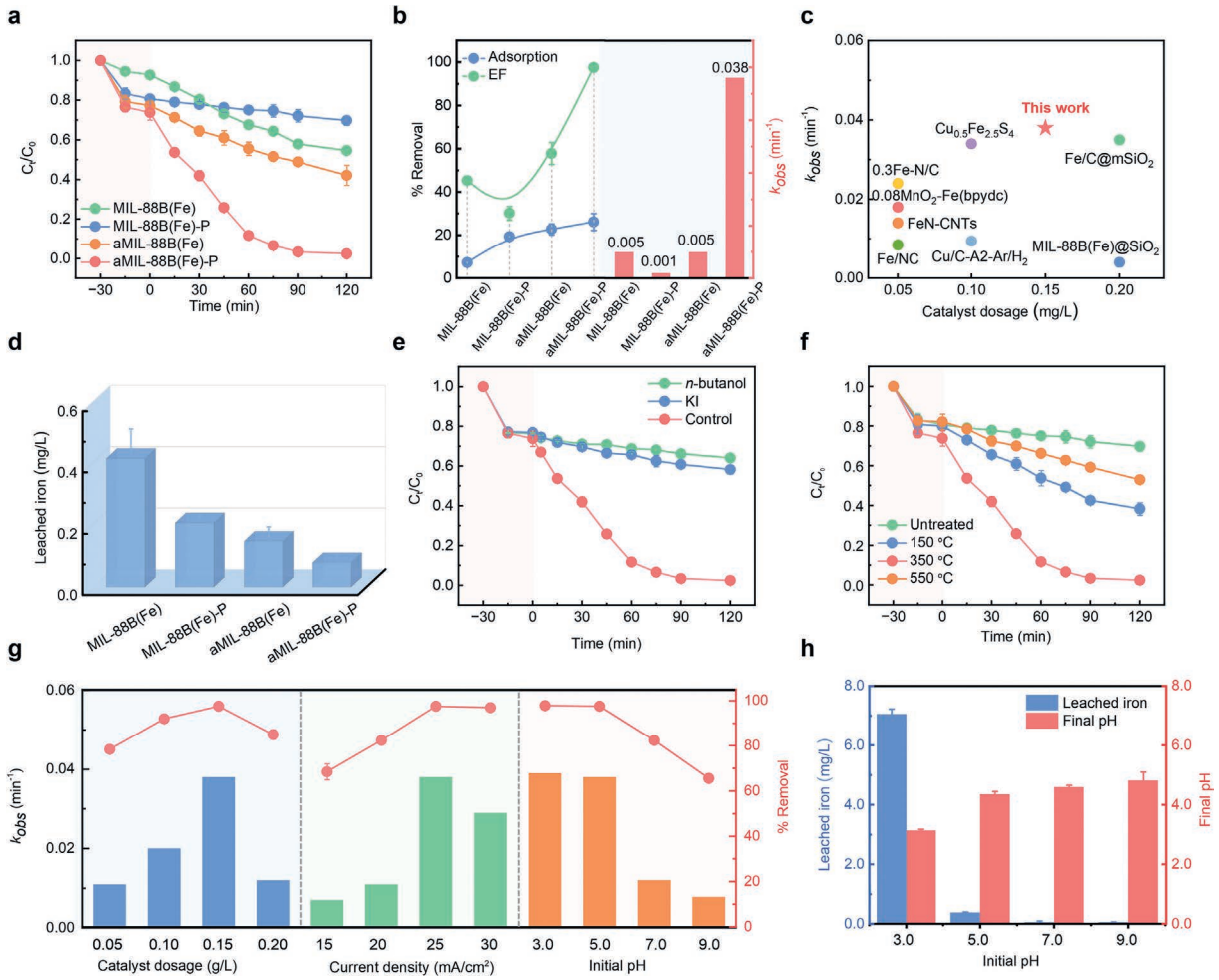


Fig. 3. (a) Normalized concentration decay of NPX in 160 mL of 0.05 mol/L Na_2SO_4 solution under EF treatment with different catalysts. (b) NPX removal efficiency and corresponding observed rate constants (k_{obs}) from the trials in (a). (c) Comparison of degradation kinetics for EF treatment of micropollutants with different catalysts [1,4,46–50]. (d) Leached iron concentrations after 120 min of electrolysis from trials shown in (a). (e) Effect of radical scavengers on NPX degradation in the aMIL-88B(Fe)-P-catalyzed EF system. (f) Influence of synthesis temperature on catalytic performance. (g) NPX removal efficiency and corresponding reaction rate constants under different influencing factors, including catalyst dosage, current density and initial pH. (h) Leached iron concentration and final pH after 120 min of electrolysis in trials with varying initial pH. General conditions unless otherwise specified: [NPX] = 10 mg/L, [Catalyst] = 0.15 g/L, [Current density] = 25 mA/cm^2, initial pH 5.0, [KI] = 10 mmol/L, [*n*-butanol] = 300 mmol/L.

30.3 % NPX removal (Figs. 3a and b). This performance decline is attributed to the compact crystalline nature of the MOF and the presence of bonded/adsorbed PPh_3 molecules, both of which restrict access of H_2O_2 and NPX to the Fe sites. In contrast, the aMIL-88B(Fe)-based EF system showed a more substantial NPX removal of 97.6 %, owing to enhanced active site accessibility and improved mass transport. Notably, the aMIL-88B(Fe)-P-catalyzed EF process outperformed all the prior systems, attaining complete NPX abatement within 90 min. The pseudo-first-order kinetic rate constant (k_{obs}) of NPX degradation over aMIL-88B(Fe)-P reached 0.038 min^{-1}, approximately eight times higher than that of the EF with aMIL-88B(Fe) (0.005 min^{-1}), and surpassing the performance of many reported HEF systems (Figs. 3b and c) [1,4,46–50]. Importantly, aMIL-88B(Fe)-P also exhibited excellent stability, with Fe leaching as low as 0.08 mg/L after 120 min treatment (Fig. 3d). This value is not only markedly lower than that observed in other catalytic systems but also well below the European Union standard of 2 mg/L. The superior catalytic activity and stability of aMIL-88B(Fe)-P result from the synergistic effects of structural amorphization and local coordination modulation. Amorphization increases the surface area and porosity, facilitating greater exposure of Fe active sites and enhancing mass transport. Meanwhile, P incorporation introduces Fe–O–P moieties, which modulate the electronic structure of the Fe centers and stabilize the catalytic sites, thereby improving both catalytic efficiency and long-term durability.

Generally, •OH generated at catalytic sites can either diffuse into the bulk solution as free radicals (*i.e.*, $^{\bullet}OH_{free}$) to react with pollutants or remain adsorbed on the surface (*i.e.*, $^{\bullet}OH_{ads}$). To identify the dominant reactive pathway, radical scavenging experiments were performed using *n*-butanol and KI as quenching agents. *n*-Butanol is capable of quenching both $^{\bullet}OH_{free}$ and $^{\bullet}OH_{ads}$, whereas KI selectively scavenges $^{\bullet}OH_{ads}$ [4]. As shown in Fig. 3e, the addition of either *n*-butanol or KI significantly suppressed NPX degradation, resulting in a similarly reduced removal efficiency of approximately 40 %. This indicates that the $^{\bullet}OH_{ads}$ plays a predominant role in NPX degradation. This finding supports the earlier hypothesis that the amorphous structure of aMIL-88B(Fe)-P promotes the enrichment of H_2O_2 and NPX within the catalyst, thereby facilitating direct NPX oxidation by $^{\bullet}OH_{ads}$ without radical diffusion into the bulk phase. Moreover, the negligible iron leaching from aMIL-88B(Fe)-P corroborates this mechanism, as it excludes the possibility of a significant contribution of homogeneous EF to NPX degradation. In addition, probe experiments using nitro blue tetrazolium (NBT) excluded the generation of

superoxide radicals ($^{\bullet}O_2^-$) in the aMIL-88B(Fe)-P-based EF system, while scavenging trials with furfuryl alcohol (FFA) confirmed the negligible contribution of singlet oxygen ($^1O_2$) to NPX degradation (Figs. S3 and S4 in Supporting information).

The temperature applied during material amorphization profoundly influences EF performance. As illustrated in Fig. 3f, the sample subjected to 150 °C heat treatment exhibited a limited NPX removal efficiency of 72.7 %, though still outperforming the pristine MIL-88B(Fe)-P. This temperature corresponds to the first weight-loss stage in the TGA profile, where physically adsorbed solvents and water molecules are gradually evaporated, but significant amorphization has yet to occur (Fig. 1f). Raising the temperature to 350 °C resulted in the formation of well-amorphized aMIL-88B(Fe)-P, which achieved the most rapid NPX degradation in the EF system. However, further increasing the temperature to 550 °C adversely affected NPX removal, yielding an efficiency of only 47.1 %. High-temperature treatment not only disrupts the crystalline structure of MOF but also induces phase transformation of Fe species into crystalline Fe_3O_4, as evidenced by XRD analysis in Fig. S5 (Supporting information), which typically shows poor activity for H_2O_2 activation. As demonstrated by Fig. S6 (Supporting information), the commercial Fe_3O_4-based EF system attained only 47.1 % NPX removal within 120 min. Moreover, such thermal treatment often causes structural collapse and severe aggregation of Fe species, further diminishing the density of accessible active sites (Fig. S7 in Supporting information). To clarify the role of PPh_3 loading, the effect of PPh_3/MIL-88B(Fe) molar ratios on NPX decay was systematically examined. As shown in Fig. S8a (Supporting information), the catalytic performance exhibited a strong dependence on the PPh_3 amount, with maximum NPX removal achieved at a ratio of 2:1. A moderate increase in the PPh_3/MIL-88B(Fe) ratio promoted the formation of P–Fe–O moieties, thereby enhancing the intrinsic catalytic activity, whereas excessive PPh_3 hampered the amorphization of MIL-88B(Fe) due to its heat insulation effect (Fig. S8b in Supporting information)

The effects of key operational parameters, including catalyst dosage and applied current density and pH, on NPX decay were investigated in the aMIL-88B(Fe)-P-catalyzed EF system (Fig. 3g). As expected, both NPX removal efficiency and the corresponding k_{obs} value initially increased with catalyst dosage, peaking at 0.15 g/L. Beyond this optimum, a noticeable decline was observed (Fig. 3g and Fig. S9 in Supporting information). This trend can be attributed to the increased availability of active sites at moderate catalyst loadings, which enhances $^{\bullet}OH$ generation and subsequent pollutant oxidation. However, a higher dosage of 0.20 g/L may lead to the scavenging of $^{\bullet}OH$ by excess iron species [51,52]. As can be seen in Fig. 3g and Fig. S10 (Supporting information), increasing the applied current density positively influenced NPX degradation, with complete removal achieved within 90 min at 25 and 30 mA/cm^2. Higher current densities enhance cathodic H_2O_2 generation, thereby promoting $^{\bullet}OH$ production for NPX destruction (Fig. S11 in Supporting information). Nevertheless, an excessively high H_2O_2 concentration can also quench $^{\bullet}OH$, leading to a slightly reduced k_{obs} value of 0.029 min^{-1} [53]. Furthermore, lower initial pH values favored NPX degradation, with the highest removal rates observed at pH 3.0 and 5.0, yielding k_{obs} values of 0.039 min^{-1} and 0.038 min^{-1}, respectively (Fig. 3g and Fig. S12 in Supporting information). However, operation at pH 3.0 resulted in significant iron leaching (6.8 mg/L after 120 min), undermining catalyst reusability and increasing the contribution of homogeneous Fenton reaction (Fig. 3h). Fortunately, aMIL-88B(Fe)-P maintained high stability and activity at near neutral pH 5.0. In contrast, its performance declined notably at pH 7.0 and 9.0, which is consistent with the pH-sensitive nature of $^{\bullet}OH$-based degradation due to the diminished oxidative potential and accelerated H_2O_2 decomposition under alkaline conditions [54]. Notably, the solution pH in all trials tended to decrease due to the formation of acidic intermediates like carboxylates (Fig. 3h).

Subsequently, the practical applicability of the aMIL-88B(Fe)-P-catalyzed EF system was comprehensively examined. As shown in Fig. 4a, over 80 % removal efficiency was achieved for each pollutant after 120 min treatment at pH 5.0, with observed k_{obs} values ranging from 0.015 min^{-1} to 0.032 min^{-1} (Fig. S13 in Supporting information). The relatively high degradation performance across diverse pollutants is ascribed to the non-selective nature of $^{\bullet}OH$-mediated oxidation, underscoring the broad applicability. The variations in degradation kinetics may arise from the differing physicochemical properties of individual pollutants [55]. The system flexibility was further assessed by introducing typical anions (NO_3^-, CO_3^{2-} and Cl^-) into the electrolyte. As depicted in Fig. 4b, the presence of Cl^- significantly enhanced NPX removal, achieving nearly complete degradation within only 60 min. This is attributed to the generation of additional reactive chlorine species (*e.g.*, Cl_2, HClO, $Cl^{\bullet-}$ and $Cl_2^{\bullet-}$) at the DSA surface, which can synergistically promote NPX oxidation [3]. In contrast, the presence of CO_3^{2-} and NO_3^- inhibited the degradation performance, likely due to their scavenging effects on $^{\bullet}OH$ [1]. Additionally, NPX degradation was evaluated in various water matrices, including urban wastewater, deionized water, tap water, lake water, and river water. The urban wastewater was collected from the secondary effluent of the Jiguanshi Wastewater Treatment Plant (Chongqing, China), with detailed water quality parameters provided in Table S1 (Supporting information). As illustrated in Fig. 4c, over 90 % NPX removal was achieved in all cases after 120 min, though slight performance inhibition was observed in urban wastewater and lake water due to the competitive consumption of $^{\bullet}OH$ by coexisting natural organic matter. These results highlight the excellent environmental adaptability of the aMIL-88B(Fe)-P-catalyzed EF system. Furthermore, the system durability was assessed over ten consecutive NPX degradation cycles at initial pH 5.0. as shown in Fig. 4d, the removal efficiency remained above 90% during the first eight cycles and declined slightly to 81.3 % by the tenth cycle, demonstrating favorable recyclability of aMIL-88B(Fe)-P. However, a gradual decline in k_{obs} was observed, decreasing from 0.038 min^{-1} in the first cycle to 0.013 min^{-1} by the tenth (Fig. 4e). This mild deactivation is ascribed to inevitable active-site blockage and slight iron aggregation during prolonged operation, as evidenced by the appearance of weak crystalline peaks in the XRD pattern of the used catalyst (Fig. S14 in Supporting information). Notably, the reusability of aMIL-88B(Fe)-P still surpasses that of many previously reported HEF systems (Fig. 4f) [4,20,40,46,48,55–60]. Although the amorphization process disrupts the MOF's compact crystalline structure, phosphorus incorporation further stabilizes the iron centers by forming new P–Fe–O coordination bonds. In addition, the superior mineralization performance of the aMIL-88B(Fe)-P-catalyzed EF system was confirmed by TOC measurements (Fig. S15 in Supporting information). After 6 h of treatment, the aMIL-88B(Fe)-P-based system achieved an 84.5 % TOC removal, markedly higher than that obtained with the aMIL-88B(Fe) counterpart (38.3 %).

The electron transfer capacity of the catalysts was systematically evaluated through chronoamperometry (*i*–*t*), linear sweep voltammetry (LSV), and electrochemical impedance spectroscopy (EIS). As shown in Fig. 5a, aMIL-88B(Fe)-P exhibited markedly enhanced cathodic current responses compared to aMIL-88B(Fe) upon the sequential addition of H_2O_2 and NPX, indicating superior electron transfer efficiency during the EF process. The sharp increase in cathodic current upon H_2O_2 injection reflects the rapid reduction of H_2O_2 to form $^{\bullet}OH$. The subsequent current response following NPX addition results from the strong interaction between NPX and $^{\bullet}OH_{ads}$, highlighting the powerful pollutant degradation capability of the aMIL-88B(Fe)-P-catalyzed EF system. Consistently, the LSV profiles reveal pronounced increases in current for aMIL-

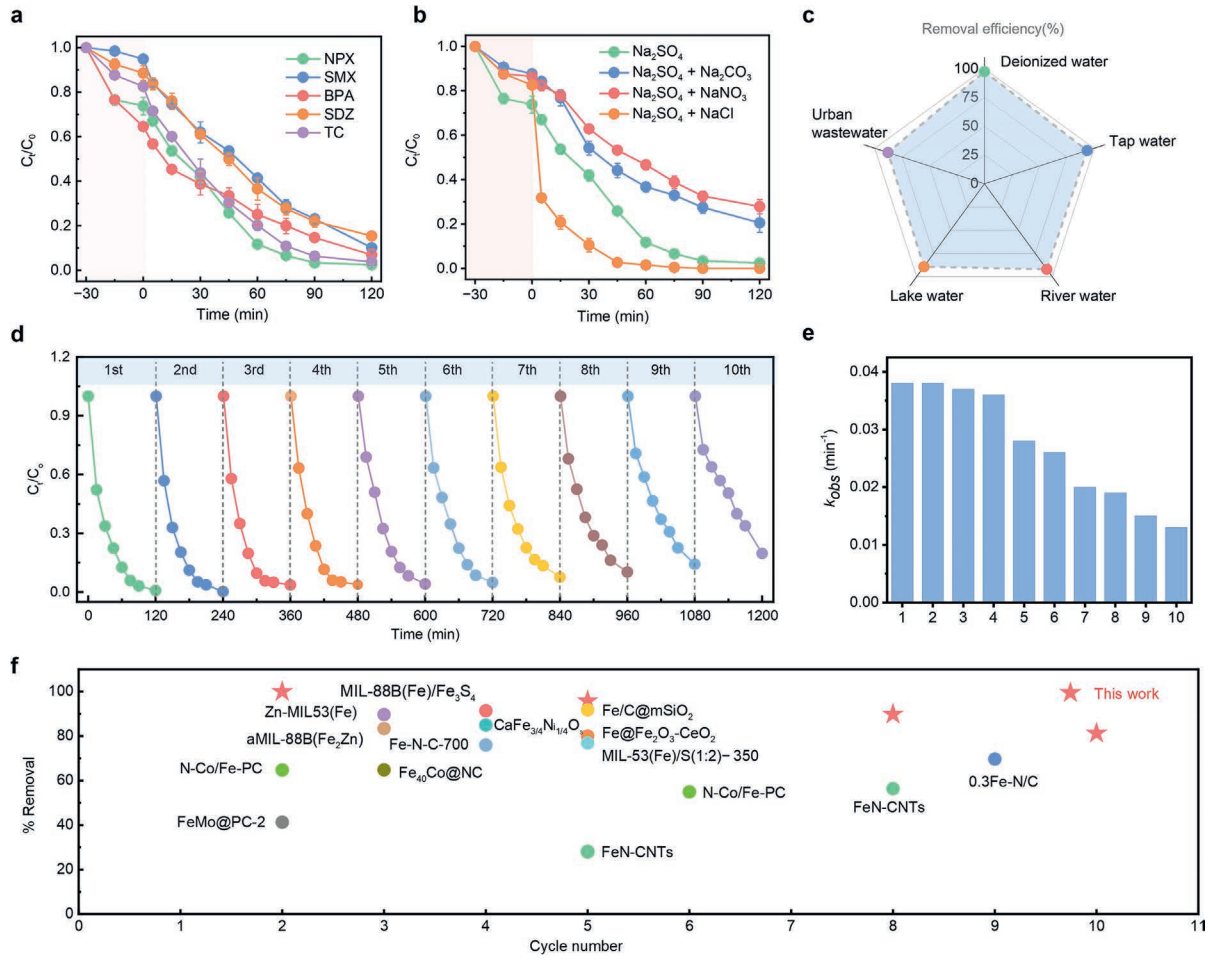


Fig. 4. (a) Degradation performance of aMIL-88B(Fe)-P-catalyzed EF system toward various micropollutants, including naproxen (NPX), sulfamethoxazole (SMX), bisphenol A (BPA), sulfadiazine (SDZ) and tetracycline (TC). Effects of (b) inorganic anions and (c) water matrices on NPX degradation in the aMIL-88B(Fe)-P-catalyzed EF system. (d) Cycling experiments for NPX degradation and (e) corresponding observed rate constants in the aMIL-88B(Fe)-P-catalyzed EF system. (f) Comparison of micropollutants degradation performance in cycling experiments across various heterogenous EF systems [4,20,40,46,48,55–60]. General conditions: [Pollutants] = 10 mg/L, [Catalyst] = 0.15 g/L, [Current density] = 25 mA/cm^2, Initial pH 5.0, and 0.05 mol/L Na_2SO_4 electrolyte unless otherwise specified. For (b): [Na_2CO_3] = 0.03 mol/L, [$NaNO_3$] = 0.03 mol/L, [NaCl] = 0.03 mol/L.

88B(Fe)-P upon sequential addition of H_2O_2 and NPX, further confirming the efficient electron transfer between aMIL-88B(Fe)-P and the reactants (Fig. 5b). In addition, Nyquist plots and the corresponding equivalent circuit diagrams were shown in Fig. 5c. aMIL-88B(Fe)-P exhibited a significantly smaller semicircle diameter and lower charge transfer resistance (R_{ct}) compared to aMIL-88B(Fe) (100 Ω *vs.* 124 Ω), underscoring its enhanced interfacial electron transfer kinetics.

Moreover, DFT calculations were performed to gain deeper insights into the underlying catalytic mechanism. The projected density of states (DOS) for Fe sites in aMIL-88B(Fe) showed notable changes upon P-incorporation (Fig. 5d). In aMIL-88B(Fe), the DOS near the Fermi level is largely suppressed, forming a pseudo-bandgap indicative of poor electronic conductivity and a localized electronic structure. In contrast, the Fe d-band center in aMIL-88B(Fe)-P shifts upward toward the Fermi level, potentially facilitating stronger interactions between the Fe sites and reaction intermediates [61]. Upon H_2O_2 adsorption, this electronic advantage of aMIL-88B(Fe)-P is retained, with both catalysts exhibiting increased DOS near the Fermi level (Figs. 5e and f). This suggests that H_2O_2 adsorption induces further electronic redistribution, enhancing orbital hybridization and charge transfer, which is conducive to accelerating the cleavage of the O–O bond in H_2O_2 for $^{\bullet}OH$ production. To further clarify the origin of the enhanced catalytic activity, the adsorption behavior of H_2O_2 on both aMIL-88B(Fe) and aMIL-88B(Fe)-P was investigated. As illustrated in Figs. 5g and h, H_2O_2 exhibits a stronger binding affinity to the asymmetric P–Fe–O coordination structure, with a more negative adsorption energy (-1.31 eV) compared to that on aMIL-88B(Fe) (-0.55 eV). This suggests that P-incorporation thermodynamically favors H_2O_2 interaction with the Fe site. These findings align with the DOS results, where the upshifted d-band center and increased DOS promote electron transfer from Fe sites to the H_2O_2 antibonding orbital.

Collectively, the amorphous structure of aMIL-88B(Fe)-P promotes the rapid diffusion of H_2O_2 and NPX toward accessible active sites. In addition, P-induced modulation of the local coordination environment enhances both the internal metal–nonmetal electron transfer and the interfacial electron exchange between the catalyst and reactants. These synergistic effects collectively accelerate $^{\bullet}OH$ production and subsequent NPX degradation (Fig. 5i).

To further elucidate the practical application capability of aMIL-88B(Fe)-P-catalyzed EF system, a flow-through electrochemical device with a custom-designed circular cathode with a diameter of 5 cm, an IrO_2-DSA anode was established (Fig. 6a). The cathode was fabricated *via* the hot-rolling method, with carbon cloth acting as the substrate to support the catalysts. A Ni mesh next to the cathode was employed as the current collector. The solution was recirculated within an external reservoir at the flow rate

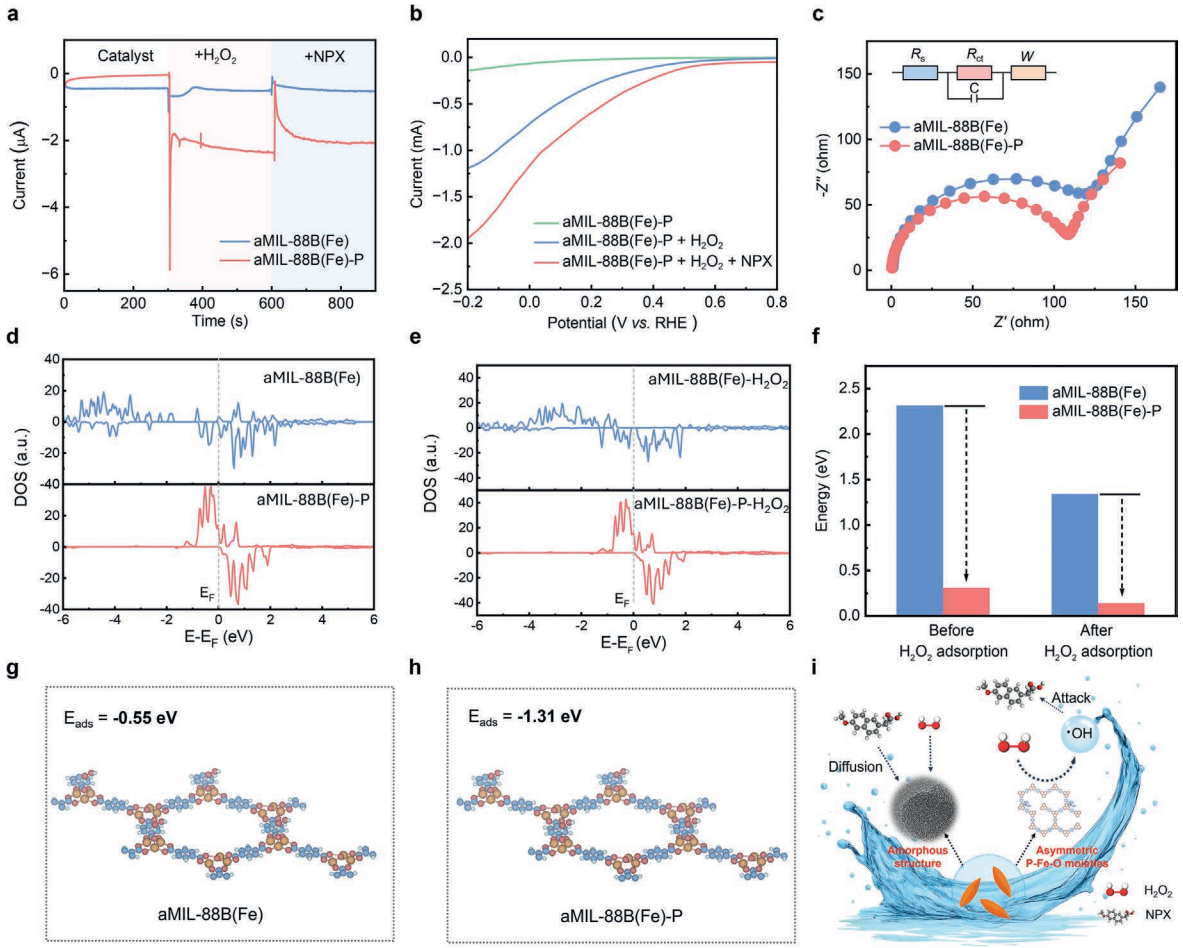


Fig. 5. (a) Chronoamperometry and (b) linear sweep voltammetry (LSV) curves for aMIL-88B(Fe) and aMIL-88B(Fe)-P upon the addition of H_2O_2 and NPX. (c) EIS plots of aMIL-88B(Fe) and aMIL-88B(Fe)-P. Density of states (DOS) of aMIL-88B(Fe) and aMIL-88B(Fe)-P (d) before and (e) after H_2O_2 adsorption. (f) Calculated d-band center of aMIL-88B(Fe) and aMIL-88B(Fe)-P with and without H_2O_2 adsorption. Optimized H_2O_2 adsorption configurations and corresponding adsorption energies on (g) aMIL-88B(Fe) and (h) aMIL-88B(Fe)-P, respectively. (i) Proposed catalytic mechanism of the aMIL-88B(Fe)-P-catalyzed EF process.

of 10 mL/min and continuously treated by pumping air to ensure sufficient O_2 supply. As depicted in Fig. 6b, the superior performance of aMIL-88B(Fe)-P-catalyzed EF system was replicated, achieving complete NPX abatement within 90 min treatment, while the aMIL-88B(Fe)-based counterpart only attained 73.5 % removal even after 120 min. This result implies the superior scalability of aMIL-88B(Fe)-P-catalyzed EF system for larger-scale wastewater treatment.

The potential environmental impact of the aMIL-88B(Fe)-P-based EF wastewater treatment system was further assessed *via* LC-MS analysis and toxicity assessment. Eleven intermediates identified by LC-MS analysis enabled the proposal of a detailed NPX degradation pathway (Fig. S16 in Supporting information). NPX underwent successive hydroxylation, decarboxylation, ring-opening, and dealkylation reactions to yield a series of intermediates (P1-P11), which were ultimately mineralized into CO_2 and H_2O. Toxicity evaluation was performed using a barley seed germination assay. As depicted in Fig. 6c, a natural control (NC) group and a pollution control (PC) group were first established. The PC group that exposed to untreated NPX solution exhibited markedly suppressed barley seed germination, highlighting the pronounced phytotoxicity of NPX. Time-course observations revealed that barley seeds in the aMIL-88B(Fe)-P/EF-treated group exhibited earlier germination onset and faster root and shoot elongation compared to those in the aMIL-88B(Fe)/EF-treated groups. By day four, seedlings in the aMIL-88B(Fe)-P/EF-treated group had developed visibly longer roots and shoots, whereas those in the PC and aMIL-88B(Fe)/EF-treated groups either failed to germinate or showed stunted growth. As shown in Fig. 6d, the germination rates in the PC (50 %) and aMIL-88B(Fe)/EF-treated (55 %) groups were significantly lower than that of the NC group (95 %), indicating residual phytotoxicity due to incomplete NPX degradation. In contrast, the germination rate in the aMIL-88B(Fe)-P/EF-treated group reached 85 %, comparable to that of the NC group, suggesting minimal residual phytotoxicity and effective detoxification. A more detailed analysis of root and shoot length inhibition rates revealed statistically significant differences among the treatments (Figs. 6e and f). The aMIL-88B(Fe)/EF-treated group showed inhibition rates of 87.7 % for roots and 87.3 % for shoots, whereas treatment with the aMIL-88B(Fe)-P-based system significantly enhanced root (49.2 %) and shoot (31.1 %) growth. This improvement is attributed to the efficient decomposition of NPX into less toxic intermediates or its complete mineralization into CO_2 and H_2O. These findings highlight the remarkable degradation and detoxification performance of the aMIL-88B(Fe)-P-based EF wastewater treatment system, underscoring its promising environmental applicability.

Based on the optimized operating parameters of the HEF system, an economic evaluation was conducted using NPX-containing wastewater as the target matrix. The synthesis cost of aMIL-88B(Fe)-P was estimated to be 0.51 USD/g (Table S2 in Supporting information), and the corresponding unit water treatment cost was 0.132 USD/L (Table S3 in Supporting information), which is comparable to similar reported electrochemical systems [62]. The overall cost was further assessed by considering the energy con-

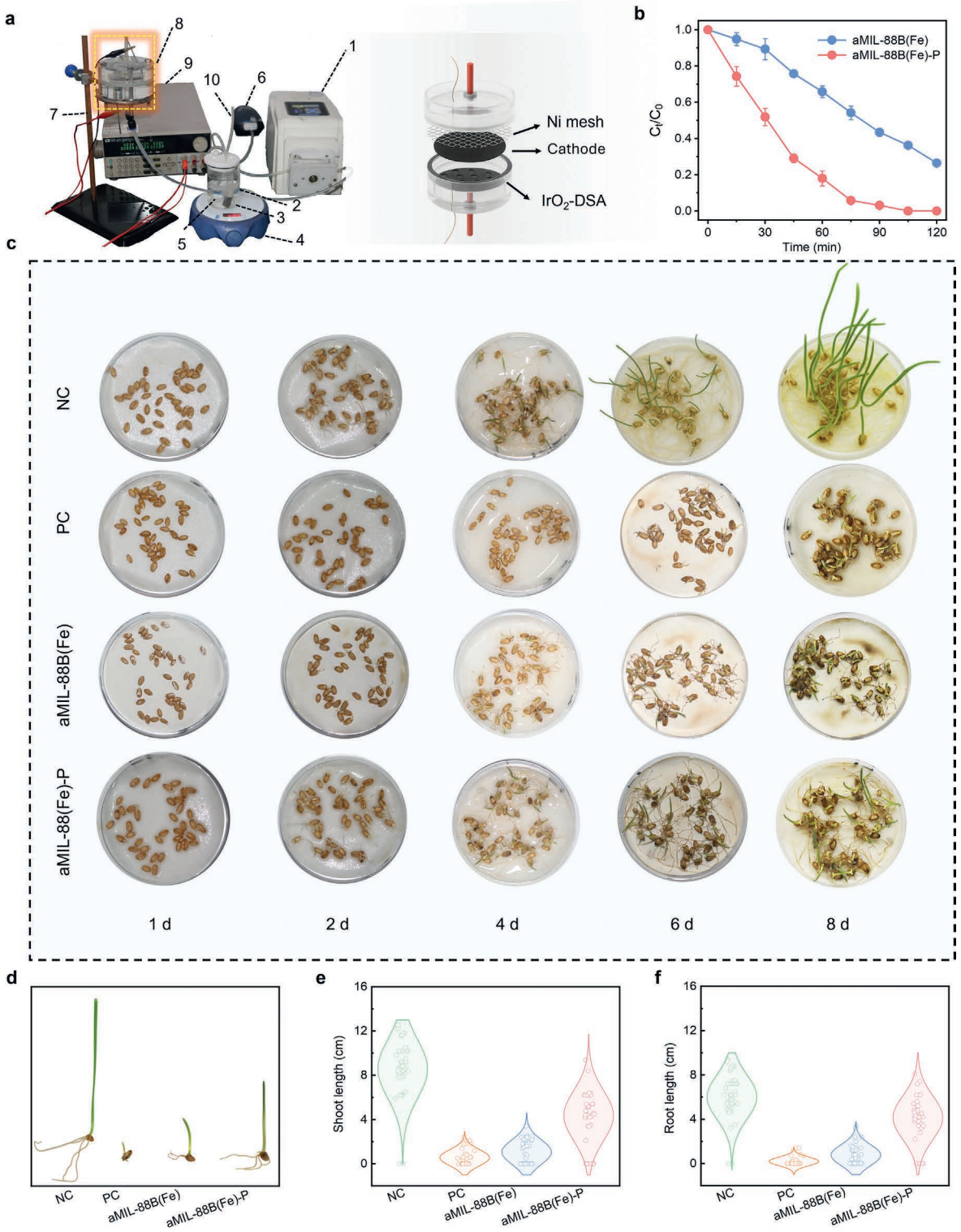


Fig. 6. (a) Photograph of the practical NPX degradation device and schematic illustration of the flow-through electrochemical cell (1, Peristaltic pump; 2, Beaker reactor; 3, Aeration diffuser; 4, Magnetic stirrer; 5, Magnetic stir bar; 6, Air pump; 7, Retort stand; 8, Electrochemical reactor; 9, DC Power; 10, Connecting wires). (b) Normalized NPX concentration decay in aMIL-88B(Fe)- and aMIL-88B(Fe)-P-catalyzed EF systems using the setup shown in (a). Volume: 100 mL, [NPX] = 10 mg/L, [Current density] = 4 mA/cm^2, initial pH = 5.0. (c) Photograph of the wheat seed germination experiment. (d) Comparison of seed growth across different systems. (e) Shoot length and (f) root length of wheat seedlings exposed to various effluents.

sumption, catalyst dosage, and supporting electrolyte under optimized conditions. Notably, the aMIL-88B(Fe)-P-catalyzed EF exhibited a markedly lower treatment cost of 13.71 USD/g, compared with 22.96 USD/g for the aMIL-88B(Fe)-based system, highlighting its superior economic feasibility.

In summary, we have developed a P-coordinated amorphous MIL-88B(Fe) catalyst *via* stepwise phosphine-functionalization and low-temperature heat treatment to construct a robust EF system for micropollutant degradation. The amorphization of MIL-88B(Fe) disrupted its compact hexagonal structure, resulting in greater

active site exposure and enhanced diffusion of H_2O_2 and NPX toward accessible catalytic centers. Moreover, the P-induced asymmetric local coordination environment significantly modulated the electron distribution, upshifting the Fe d-band center toward the Fermi level. This electronic fine-tuning enhanced H_2O_2 adsorption and lowered the activation energy barrier. In addition, P-doping stabilized the iron active sites, partially compensating for the reduced structural robustness caused by the loss of crystallinity. Consequently, the aMIL-88B(Fe)-P-catalyzed EF system achieved complete naproxen abatement within 90 min, outperforming all comparative trials and many reported heterogenous EF systems. Furthermore, the system demonstrated excellent durability, robust resistance to complex water matrices, and broad applicability for diverse micropollutants degradation. Analysis of the NPX degradation pathway and toxicity assays further confirmed its high potential for practical applications in refractory wastewater treatment.

CRediT authorship contribution statement

Pan Xia: Writing – original draft, Methodology, Investigation, Data curation, Conceptualization. **Chuanzhu Tang:** Validation, Methodology, Investigation, Data curation, Conceptualization. **Tong Xu:** Methodology, Investigation, Data curation. **Pinyuan Sheng:** Validation, Methodology, Data curation. **Liyuan Liu:** Validation, Methodology, Data curation. **Chao Wang:** Validation, Methodology, Investigation. **Yin Xu:** Supervision, Methodology, Investigation. **Qiang He:** Supervision, Resources. **Ömür Gökkuş:** Supervision, Methodology, Investigation. **Zhihong Ye:** Writing – review & editing, Supervision, Project administration, Methodology, Investigation, Funding acquisition, Conceptualization.

Declaration of competing interest

The authors declare that they have no known competing financial interests or personal relationships that could have appeared to influence the work reported in this paper.

Acknowledgments

The authors gratefully acknowledge the National Natural Science Foundation of China (No. 52100073), the Natural Science Foundation of Chongqing (No. CSTB2022NSCQ-MSX0432), Graduate Scientific Research and Innovation Foundation of Chongqing (No. CYB25050), and the Venture and Innovation Support Program for Chongqing Overseas Returnees (No. cx2022048).

Supplementary materials

Supplementary material associated with this article can be found, in the online version, at doi:10.1016/j.cclet.2026.112442.

References

[1] C. Wang, W. Zhang, J. Wang, et al., Appl. Catal. B: Environ. 342 (2024) 123457.
[2] J. Qu, J. Liu, N.A. Al-Dhabi, et al., Sep. Purif. Technol. 376 (2025) 133980.
[3] P. Xia, Z. Chen, D. Wang, et al., Sep. Purif. Technol. 319 (2023) 124035.
[4] J. Wang, H. Li, P. Xia, et al., Chem. Eng. J. 483 (2024) 149230.
[5] T. Hu, W. Zhou, W. Tang, Coordin. Chem. Rev. 526 (2025) 216357.
[6] X. Wu, J. Lu, Z. Zhu, S. Liu, H. Ren, Chin. Chem. Lett. 36 (2025) 110151.
[7] H. Fu, C. Wang, W. Liu, Chin. Chem. Lett. 33 (2022) 1647–1649.
[8] C. Cao, S. Chen, X. Quan, H. Yu, Y. Zhang, J. Catal. 356 (2017) 125–132.
[9] W. Niu, Y. Yang, ACS. Appl. Energy Mater. 1 (2018) 2440–2445.
[10] W. Yang, Z. Zhang, J. Wu, et al., JACS. Au 5 (2025) 1184–1195.
[11] Z. Ye, R. Oriol, C. Yang, I. Sirés, X. Li, Chem. Eng. J. 433 (2022) 133547.
[12] J. Chen, Y. Wang, J. Huang, et al., Catalysts 15 (2024) 220.
[13] P. Xia, C. Wang, Q. He, et al., Chem. Eng. J. 452 (2023) 139446.
[14] X. Lu, P. Su, Chin. Chem. Lett. 36 (2025) 110909.
[15] W. Tu, Y. Xu, S. Yin, R. Xu, Adv. Mater. 30 (2018) 1707582.
[16] G. Zhou, X. Zhou, J. Li, et al., Small 20 (2024) 2404598.
[17] J. Fonseca, T. Gong, L. Jiao, H. Jiang, J. Mater. Chem. A 9 (2021) 10562–10611.
[18] J. Wang, R. Huang, W. Qi, et al., Chem. Eng. J. 434 (2022) 134677.
[19] H. Wu, S. Huang, F. Ding, et al., J. Phys. Chem. C 126 (2022) 19715–19725.
[20] Z. Xu, R. Teng, L. Xu, H. Zhang, B. Lv, Adv. Funct. Mater. 34 (2024) 2401248.
[21] G. Zhu, X. Fan, Y. Yu. Y. Liu, X. Quan, Environ. Sci. Technol. 58 (2024) 19545–19554.
[22] P. Xia, Z. Ye, L. Zhao, et al., Appl. Catal. B: Environ. 322 (2023) 122116.
[23] J. Sun, H. Xue, L. Lu, et al., Appl. Catal. B: Environ. 313 (2022) 121429.
[24] Z. Tan, P. Cao, S. Chen, et al., Appl. Catal. B: Environ. Energy 355 (2024) 124170.
[25] X. Qin, P. Cao, X. Quan, et al., Environ. Sci. Technol. 57 (2023) 2907–2917.
[26] S. Liu, P. Zhang, J. Huang, et al., Sep. Purif. Technol. 326 (2023) 124843.
[27] Y. Chen, H. Kang, M. Cheng, et al., Adv. Funct. Mater. 34 (2024) 2309223.
[28] Y. Yang, M. Tan, G. Cao, et al., Chem. Eng. J. 506 (2025) 160033.
[29] L. Wang, Y. Zhang, X. Li, et al., Sci. Rep. 5 (2015) 14341.
[30] M. Ma, A. Bétard, I. Weber, et al., Cryst. Growth Des. 13 (2013) 2286–2291.
[31] X. Zhang, H. Li, X. Lv, et al., Chem. Eur. J. 24 (2018) 8822–8832.
[32] M. Morsy, S.S. Hassan, H.M. Shaker, K.M. Ismail, Sens. Actuators B 438 (2025) 137806.
[33] X. Yang, L. Zhou, P. Tan, et al., ACS. Nano 17 (2023) 19275–19287.
[34] N. Liu, J. Wu, F. Fei, et al., J. Colloid. Interface Sci. 612 (2022) 1–12.
[35] D. Pukazhselvan, C.M. Granadeiro, F.J.A. Loureiro, et al., Electrochim. Acta 465 (2023) 142989.
[36] X. Cai, Y. Tian, H. Wang, Angew. Chem. Int. Ed. 137 (2025) e202414030.
[37] W. Yan, S. Li, T. Yang, et al., J. Am. Chem. Soc. 142 (2020) 16182–16187.
[38] H. Jin, Z. Kou, W. Cai, et al., J. Mater. Chem. A 8 (2020) 9121–9127.
[39] J. Bai, J. Xu, Z. Sun, et al., J. Phys. Chem. Lett. 16 (2025) 6833–6840.
[40] Z. Ye, W. Zhang, S. Lanzalaco, et al., Chem. Eng. J. 455 (2023) 140757.
[41] X. Cheng, Y. Bi, X. Liu, et al., Adv. Funct. Mater. 35 (2025) 2413883.
[42] S. Chen, T. Luo, X. Li, et al., J. Am. Chem. Soc. 144 (2022) 14505–14516.
[43] S. Huang, F. Lin, S. Wang, et al., Adv. Mater. 36 (2024) 2407974.
[44] N. Wang, R. Mei, L. Chen, et al., Small 20 (2024) 240032.
[45] W. Xue, Q. Zhou, X. Cui, et al., Angew. Chem. Int. Ed. 62 (2023) e202307504.
[46] J. Guo, G. Song, M. Zhou, Chem. Eng. J. 474 (2023) 145681.
[47] L. Zhao, J.A. Padilla, E. Xuriguera, et al., Chemosphere 364 (2024) 143249.
[48] L. Zhao, M.F. Murrieta, J.A. Padilla, et al., Sci. Total. Environ. 953 (2024) 176110.
[49] J. Guo, G. Song, Y. Zheng, et al., Sep. Purif. Technol. 302 (2022) 122141.
[50] J. Lin, Y. Huang, L. Fan, et al., Electrochim. Acta 537 (2025) 146818.
[51] J. Zhang, S. Qiu, H. Feng, et al., Chem. Eng. J. 428 (2022) 131403.
[52] Y. Yang, B. Yang, X. Gao, et al., J. Water. Process. Eng. 72 (2025) 107467.
[53] X. Du, W. Fu, P. Su, et al., Chem. Eng. J. 398 (2020) 125681.
[54] X. Li, C. Wang, P. Xia, et al., Electrochim. Acta 524 (2025) 145974.
[55] J. Guo, Y. Wang, Y. Shang, et al., Proc. Natl. Acad. Sci. U. S. A. 121 (2024) e2313387121.
[56] L. Qin, W. Chen, Y. Fu, et al., Chem. Eng. J. 449 (2022) 137840.
[57] D. Terrón, J.P. Holgado-Vázquez, E. Rosales, et al., Sep. Purif. Technol. 360 (2025) 130881.
[58] C. Sun, J. Wang, C. Gu, et al., Chem. Eng. J. 45 (2023) 139592.
[59] X. Du, W. Fu, P. Su, J. Cai, M. Zhou, J. Hazard. Mater. 424 (2022) 127674.
[60] Y. Liang, A. Feng, N.A. Al-Dhabi, et al., Water. Res. 279 (2025) 12343.
[61] Y. Li, Y. Ding, B. Zhang, et al., Energy Environ. Sci. 16 (2023) 2629–2636.
[62] N. Fu, S. Li, X. Zhou, et al., J. Environ. Chem. Eng. 13 (2025) 118816.